Ultrasonics 141 (2024) 107336

Contents lists available at ScienceDirect

Ultrasonics

journal homepage: www.elsevier.com/locate/ultras

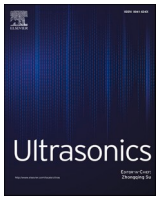

Discrete element method modelling of elastic wave propagation in a meso-scale model of concrete

Magdalena Knak [a], Michał Nitka [b], Magdalena Rucka [a,*]

[a] Department of Mechanics of Materials and Structures, Faculty of Civil and Environmental Engineering, Gdańsk University of Technology, Narutowicza 11/12, 80-233 Gdańsk, Poland
[b] Department of Engineering Structures, Faculty of Civil and Environmental Engineering, Gdańsk University of Technology, Narutowicza 11/12, 80-233 Gdańsk, Poland

ARTICLE INFO

Keywords:
Ultrasonics
Elastic wave propagation
Discrete element method
Concrete, *meso*-scale model

ABSTRACT

This paper deals with the accurate modelling of ultrasonic wave propagation in concrete at the mesoscopic level. This was achieved through the development of a discrete element method (DEM) model capable of simulating elastic wave signals comparable to those measured experimentally. The main objective of the work was to propose a novel methodology for constructing a meso-scale model of concrete dedicated to the analysis of elastic wave propagation. All the material parameters necessary to prepare a numerical DEM model of concrete at the mesoscopic level were explored and explained. Calibration of the mechanical parameters of the DEM model to match the experimental values involved linking the local, micro-parameters between particles with the global response of the whole sample. The developed numerical model was further used to simulate the propagation of elastic waves in a cubic concrete sample, in the frequency range of 100–500 kHz. The results of the DEM calculations showed good agreement with the experimental ultrasonic signals.

1. Introduction

Ultrasonic waves are widely used in non-destructive testing (NDT) and structural health monitoring applications. The ultrasonic guided wave technique has already been successfully applied to the damage detection of thin-walled structures such as metallic plates [1], composite panels [2,3], adhesive joints [4], bolted connections [5] and many others [6]. Ultrasonic techniques have also been widely used in the non-invasive diagnostics of masonry [7], concrete [8,9], timber [10,11] or rammed earth structures [12]. Nowadays, determining the exact location of the damage or the moment of its initiation becomes a major challenge for modern damage detection algorithms and SHM systems utilizing ultrasonic waves. Therefore, a currently popular approach is to support diagnostic methods with numerical simulations in order to improve the interpretation of experimental results, which are usually obtained with a limited number of detection points.

Numerical modelling of elastic wave propagation has attracted the attention of researchers in the field of NDT support. Different techniques are used depending on the problem being investigated. In general, the problem of modelling ultrasonic wave propagation is challenging because of the need for fine discretisation and a sufficiently small time step. One of the most efficient approaches is the use of a semi-analytical technique in the frequency domain, the so-called frequency domain spectral element method (FDSEM) [13]. However, this technique is limited to the analysis of simple 1D or 2D structures due to the difficulties in modelling finite length structures [14]. Therefore, the finite element method is usually used to analyse complex 3D structures. The advantage of the FEM is the availability of numerous commercial codes and its great ability to analyse structures with complicated geometry or heterogeneous internal structure. On the other hand, the application of the FEM to model wave propagation in the ultrasonic frequency range requires a very dense FE mesh resulting in long computation times. The improvement of the finite element method can be achieved by using special elements, with higher order interpolating polynomials. Such an approach is called (depending on the source) time-domain spectral finite element method (TDSEM), spectral finite element method (SFEM) or simple spectral element method (SEM) [14–16]. The main difference between FEM and SFEM lies in the choice of interpolation nodes. In the SEM, the element nodes are usually distributed according to the Gauss-Lobatto-Legendre quadrature rule. As a result, it is possible to obtain a diagonal element level mass matrix, which leads to efficient time integration. The spectral finite element method has been proven to be a helpful tool in many successful damage detection applications, such as the identification of different-sized delamination within laminates [17]

* Corresponding author.
E-mail addresses: magdalena.knak@pg.edu.pl (M. Knak), michal.nitka@pg.edu.pl (M. Nitka), magdalena.rucka@pg.edu.pl (M. Rucka).

https://doi.org/10.1016/j.ultras.2024.107336
Received 2 January 2024; Received in revised form 25 March 2024; Accepted 27 April 2024
Available online 28 April 2024

or the simulation of ultrasonic guided wave propagation in the fibres [18]. There have been some attempts to model wave propagation in concrete subjected to mechanical degradation using SFEM, but these have been limited in scope to a rough approximation of the micro-crack zone inside the beam by a reduced Young's modulus distributed according to some spatial function [19].

Accurate modelling of ultrasonic wave propagation in concrete, a material with a heterogeneous structure, requires a different approach. Meso-scale models of concrete (i.e. models in which concrete is treated as a multiphase system) have attracted the interest of researchers investigating various aspects of damage detection methods based on ultrasonic wave propagation. Asadollahi and Khazanovich [20] studied numerically the effect of aggregate shape and size on the scattering attenuation of shear waves in concrete. They developed a 3D numerical tool based on the elastodynamic finite integration technique. Yu et al. [21] employed a two-dimensional numerical model in the time domain based on a spectral element method. The model included a region of circular or polygonal scatterers randomly distributed between two homogeneous regions. The authors showed that the orientation of the aggregates has a significant effect on the coherent wave parameters. Xu et al. [22] studied the detection of debonding defects in concrete-filled steel tubes both experimentally and numerically using ultrasonic waves induced by PZT transducers. They used a *meso*-scale FEM model of concrete consisting of circular aggregates, mortar and interface transition zones. Chen et al. [23] validated the feasibility of detecting interfacial debonding using *meso*-scale numerical analysis and the multichannel analysis of surface waves (MASW) approach. For the stress wave propagation, the FEM model with the dimensions of 1 m × 1 m, and with the number of elements up to 1 000 000 was used. Equivalent homogenisation was introduced to reduce the computational time.

In recent years, great progress has been made in the development of concrete models based on the discrete element method (DEM). As concrete has a particular structure that is heterogeneous and discontinuous, the DEM is a numerical approach particularly suitable for studying its mechanical behaviour, including material *meso*-structure and cracks. A large number of works have reported on the effectiveness of the DEM in characterising fracture in concrete, e.g. [24–28]. However, studies of wave propagation modelling are still rare and limited to rock or granular materials. Sadd et al. [29] presented analyses of DEM-based simulations of wave propagation in granular materials, composed of assemblies of spherical particles and circular discs. The results showed the relationship between the wave velocity and the stiffness of the interparticle contacts. Nishida et al. [30] performed numerical DEM simulations of wave propagation in an ordered array of mono-sized spheres. The motion and normal contact forces of the particle array were analysed. Rojek et al. [31] demonstrated the ability of the discrete element method to model wave propagation in solid materials. They numerically analysed elastic wave propagation in a rock-like cohesive material. They found that the elastic properties obtained from the DEM dynamic analysis were in agreement with those obtained from the DEM simulation in the quasi-static compression test. To the best of the authors' knowledge, there is no accurate DEM model capable of simulating elastic wave signals comparable to those measured experimentally.

The study presents a comprehensive investigation of the propagation of ultrasonic waves in concrete. The main objective of the paper was to explore all the parameters necessary to create a numerical DEM model of concrete at a mesoscopic level. Such a discrete model is crucial for further application in non-destructive testing and fracture monitoring of cementitious composites. A novel algorithm for modelling and calibration of ultrasonic waves in concrete samples has been proposed. The main focus has been on the development of a step-by-step approach leading to an effective modelling of ultrasonic waves in a DEM environment.

The paper is structured as follows: Section 1 is the introduction and briefly describes the modelling methods for elastic wave propagation. Section 2 provides the fundamentals of discrete element modelling and the developed framework for modelling elastic wave propagation using DEM. Section 3 describes the determination of material parameters in static and dynamic tests for DEM modelling. After that, the calibration of local, micro-parameters between particles was explained. The numerical DEM model was then applied in Section 4 to model elastic wave propagation in concrete cubic samples. Some concluding remarks are contained in Section 5.

2. Formulation of DEM for concrete

2.1. Fundamentals of DEM

The numerical analysis was performed in the Yade software [32], which is based on the discrete element method (DEM). DEM is a computational technique used to model and analyse the behaviour of granular materials and particulate systems, including concrete. It focuses on the simulation of individual particles and their interactions in order to understand the macroscopic behaviour of materials. Using an explicit time-stepping scheme, the particles in the DEM interact with each other during translational and rotational motions using a contact law and Newton's 2nd law of motion [33,34].

The mechanical response of the DEM is shown in Fig. 1. A linear normal contact model was applied for compression. The interaction force vector between two spherical discrete elements in contact was split into normal and tangential components. Cohesive bonding was considered at the grain contacts, resulting in brittle failure under a critical normal tensile load. Tensile failure resulted in contact separation, while shear cohesion failure initiated contact slip and sliding, following the Coulomb friction law under normal compression. Linear elastic behaviour was assumed prior to reaching the fracture condition (see Fig. 1). The contact forces were related to displacements by the normal and tangential stiffness moduli, K_n and K_s. The forces acting on individual elements can be calculated using the following equations:

$$\boldsymbol{F}_n = K_n(U - U_o)\boldsymbol{N}, \tag{1}$$

$$\boldsymbol{F}_s = \boldsymbol{F}_{s,prev} + K_s \Delta \boldsymbol{X}_s, \tag{2}$$

where $\boldsymbol{F}_n$ is the normal contact force, U is the overlap between discrete elements (U_o is the initial overlap, before the test), $\boldsymbol{N}$ is the unit normal vector at the contact point, $\boldsymbol{F}_s$ is the tangential contact force, $\boldsymbol{F}_{s,prev}$ is the tangential contact force in the previous iteration, $\boldsymbol{X}_s$ is the relative tangential displacement increment (Fig. 1a), K_n is the normal contact stiffness, K_s is the tangential contact stiffness.

The initial overlap U_o was extracted from the calculated overlap at each step. This allows for the preparation of denser samples, which is an important consideration in concrete calculations. The stiffness K_n and K_s depend on the radii of the elements in contact (R_A and R_B), the Young modulus of the contact (E_{dem}), and the ratio between normal and tangential stiffness (ν_{dem}), sometimes referred to as the Poisson's ratio of the contact. These values can be obtained from the following equations:

$$K_n = E_{dem}\frac{2R_AR_B}{R_A + R_B} \text{ and } K_s = \nu_{dem}E_{dem}\frac{2R_AR_B}{R_A + R_B} \tag{3}$$

Note that E_{dem} and ν_{dem} are local, micro-parameters between particles. It is often difficult, if not impossible, to determine these parameters for concrete in the laboratory. The widely used method for determining E_{dem} and ν_{dem} is the trial-and-error technique, which involves determining the global response of the whole sample and comparing it with laboratory experiments. However, the global response (E_{glob} and ν_{glob}) depends not only on the local parameters (E_{dem} and ν_{dem}), but also on the initial porosity, the initial coordination number, the element size, and the distance to neighbouring elements. Therefore, the entire process of determining the parameters by the trial-and-error method can be quite time-consuming.

The model postulates a cohesive bond at the grain contact, with a brittle failure below the critical normal tensile force. Under normal

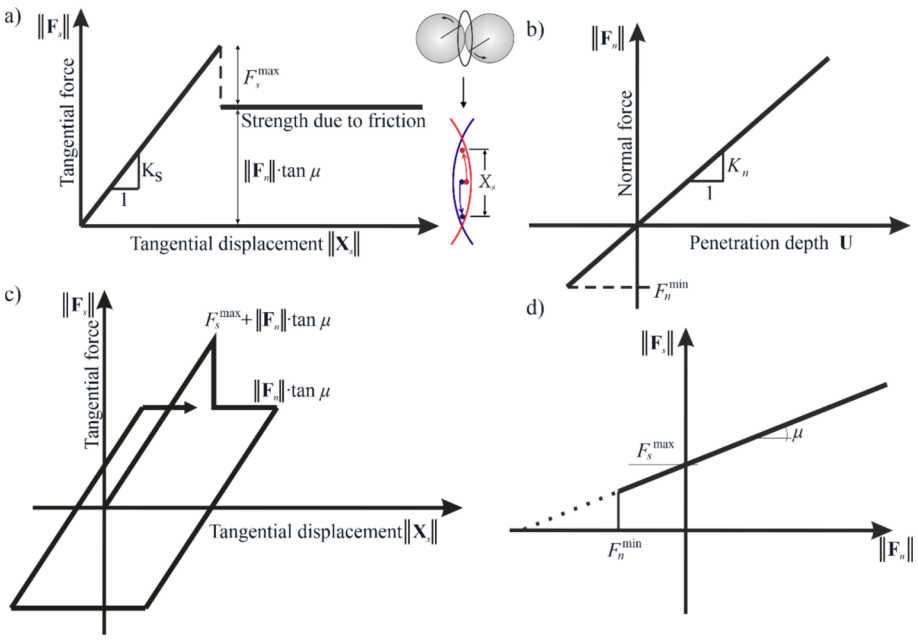

Fig. 1. Mechanical response of DEM: (a) tangential contact model, (b) normal contact model, (c) loading and unloading path in tangential contact model and (d) modified Mohr-Coulomb model [32,34].

compression, shear cohesion failure leads to contact slip and sliding, which follows the Coulomb friction law, in the following situations, namely, before contact breakage:

$$\|\boldsymbol{F}_s\| - F_s^{\max} - \|\boldsymbol{F}_n\| \times \tan\mu \leqslant 0, \tag{4}$$

and after contact breakage:

$$\|\boldsymbol{F}_s\| - \|\boldsymbol{F}_n\| \times \tan\mu \leqslant 0, \tag{5}$$

where μ is the Coulomb inter-particle friction angle and $F_s^{\max}$ is the critical cohesive contact force. The parameters used in the DEM were re-calibrated to obtain a global response consistent with the experimental results. The forces (critical cohesive contact force $F_s^{\max}$ and minimum tensile force $F_n^{\min}$) in the numerical method were calculated as follows:

$$F_s^{\max} = CR^2 \text{ and } F_n^{\min} = TR^2, \tag{6}$$

where R is the smaller radius of the spheres in contact, C is the cohesive contact stress (maximum shear stress at zero pressure), and T is the normal tensile contact stress. Failure occurs when the cohesive bond between the spheres (Eq.(6)) disappears after a critical threshold is reached. When the normal force between two elements exceeds the level of $F_n^{\min}$, the contact is broken and the normal force is equal to zero. If a shear force exceeds $F_s^{\max}$, the cohesion is broken but the contact can still exist. If a contact between spheres re-appears after failure, the cohesion is no longer present (Eq. (5)). A crack was considered to be open if the cohesive forces between grains disappeared when a critical threshold was reached. The choice of a very simple linear elastic normal contact was intended to capture, on average, the different contact possibilities in real concrete. Note that material softening is not taken into account in the DEM model. In order to dissipate the excess kinetic energy in a discrete system, a simple local non-viscous damping scheme was adopted [33], which assumed a change of forces by using the damping parameter α_d:

$$\boldsymbol{F}_{damp}^k = \boldsymbol{F}^k - \alpha_d \cdot sgn\left(\boldsymbol{v}_p^k\right)\boldsymbol{F}^k \tag{7}$$

where $\boldsymbol{F}_{damp}^k$ is the damped contact force, $\boldsymbol{F}^k$ and $\boldsymbol{v}_p^k$ are the k^{th} components of the residual force and the translational particle velocity, respectively, and α_d is the positive damping coefficient less than 1 (sgn (•) that returns the sign of the k^{th} component of the velocity).

In the general case, the mutual configuration of two particles has 6 degrees of freedom (DoFs), similar to a beam in 3D space. Each particle has 6 DoFs, while the interaction itself is free to move and rotate in space with both spheres, also having 6 DoFs: normal straining (1 DoF), shearing (2 DoFs), twisting (1 DoFs) and bending (2 DoFs).

The following material constants: E_{dem}, ν_{dem}, μ, C, and T are required for DEM simulations. In addition, R, ρ (mass density) and α_d are needed. The accuracy of the model depends on many factors, including the number and size of the elements, the number of initial contacts, whether the calculations are performed in 2D or 3D, and the time step used. The DEM model has been successfully used by the authors to describe the behaviour of concrete materials [25–27]. It has shown excellent agreement with experimental data from a mechanical point of view (e.g., stress–strain curves, crack patterns). In this study, wave propagation signals were directly compared with experimental data to ensure accurate modelling. However, incorporation of the precise *meso*-structure of the specimens analysed would improve accuracy.

2.2. Framework of modelling using DEM

The phenomenon of wave propagation using the DEM is a complex problem that is influenced by various factors. In this study, we present a methodology for constructing an appropriate *meso*-scale model of concrete dedicated to the analysis of elastic wave propagation. Fig. 2 illustrates a schematic overview summarizing the experimental investigations required and the calibration process of the numerical model. This scheme provides the basis for the development of a 3D numerical model that accurately represents the real object. The elements depicted in the diagram (experimental investigations and Yade DEM modelling) will be discussed in detail in the following sections.

The following description outlines a step-by-step approach for carrying out thorough experimental investigations and modelling:

- Step 1: determining the density of a concrete sample. The dimensions of a specimen and its mass are measured, and the density is then calculated using the formula $\rho = m/V$.
- Step 2: identification of the porosity.

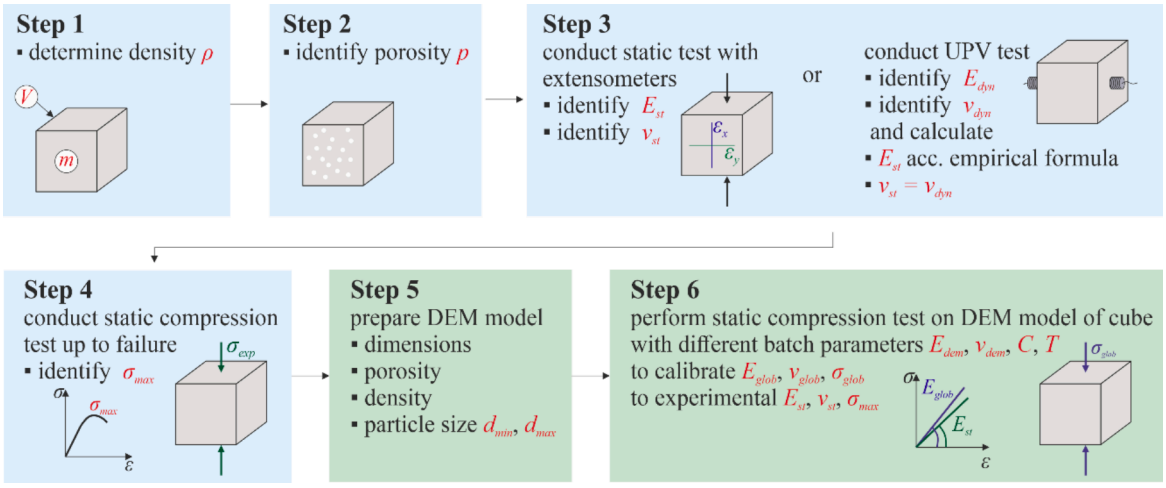

Fig. 2. A flowchart depicting steps required for the calibration of the DEM model for wave propagation.

- Step 3: identification of the static mechanical parameters, i.e., static Young modulus and static Poisson's ratio. This can be realized in two ways. The first is to perform a static compression test using two extensometers (longitudinal and transverse) to obtain directly the static Young modulus E_{st} and static Poisson's ratio ν_{st}. The second approach is to determine the dynamic parameters (E_{dyn}, ν_{dyn}) in the ultrasonic pulse velocity (UPV) test, based on the velocities of the propagating longitudinal and transverse waves. The empirical formula is then used to calculate the static modulus of elasticity E_{st}. In this approach, the dynamic Poisson's ratio is usually approximated to the static one.
- Step 4: conducting static compression test up to failure to identify the maximum stress value σ_{max}.
- Step 5: creation of a DEM model. The physical parameters required for the numerical model, such as dimensions, porosity, and density are taken from the experimental investigation. Additionally, the particle sizes d_{min} and d_{max} should be selected.
- Step 6: calibration of the mechanical parameters to match the experimental values of E_{st} and ν_{st}. This is done by performing a static compression test on the DEM cube model. By selecting appropriate batch parameters E_{dem} and ν_{dem}, the global values of E_{glob}, ν_{glob} were obtained. The calculated global stress (σ_{glob}) also needs to be calibrated to match the experimental value (σ_{max}).

3. Determination of mechanical parameters for DEM modelling

3.1. Object of research

The test objects were cubes with dimensions of 50 × 50 × 50 mm^3 and 150 × 150 × 150 mm^3. The specimens were made of concrete with only fine aggregate (so-called mortar concrete). The ingredients of the concrete mix were as follows: CEM I 42.5R (500 kg/m^3), sand 0-2 mm (1500 kg/m^3) and water (250 kg/m^3). The samples were prepared in 150 × 150 × 150 mm^3 moulds, and then some of them were cut into cubes of 50 × 50 × 50 mm^3. Before the tests, the geometry and mass of the cubes were measured to determine the density, which was ρ = 2129.56 kg/m^3. The porosity was determined on a 50 × 50 × 50 mm^3 cube. This was the same cube that was then used for the wave propagation tests. Two methods were applied to determine the porosity. The first was an optical method based on the microscopic images of the outer surfaces of the cube (Fig. 3a). Before the images were taken, the pores were filled with white plaster compound to provide better contrast. The images were taken using a Keyence VHX-7000 digital optical microscope and then processed to count the area of the pores. The second approach was based on the micro-CT method. The cube was scanned using a

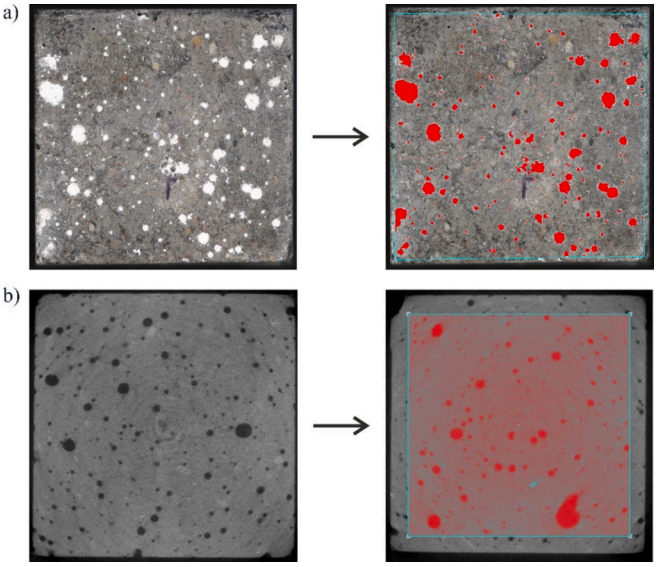

Fig. 3. Determination of porosity: (a) using a microscopic image; (b) using the micro-CT method.

SkyScan 1173 scanner. After the reconstruction process, images of the internal cross-sections were obtained (Fig. 3b). A thresholding technique based on density differences was implemented to distinguish pores from concrete in the images. Example images with identified pores on the outer surface and internal cross-section are shown in Fig. 3. Using both methods, the air content was determined to be approximately $p = 7$ %.

3.2. Determination of material parameters in static and dynamic tests

The compressive strength, modulus of elasticity and Poisson's ratio are the mechanical parameters of concrete that need to be determined for DEM modelling. The modulus of elasticity of concrete can be determined using the classical compression test. The modulus determined in this way is called the static modulus of elasticity. Extensometers, which measure longitudinal deformation, are commonly used for this purpose. Measurement of the transverse deformation required to determine Poisson's ratio is less common and is usually performed using foil strain gauges, which is more time-consuming. Therefore, the dynamic method of determining Young's modulus and Poisson's ratio by non-destructive evaluation has become popular in recent years. The

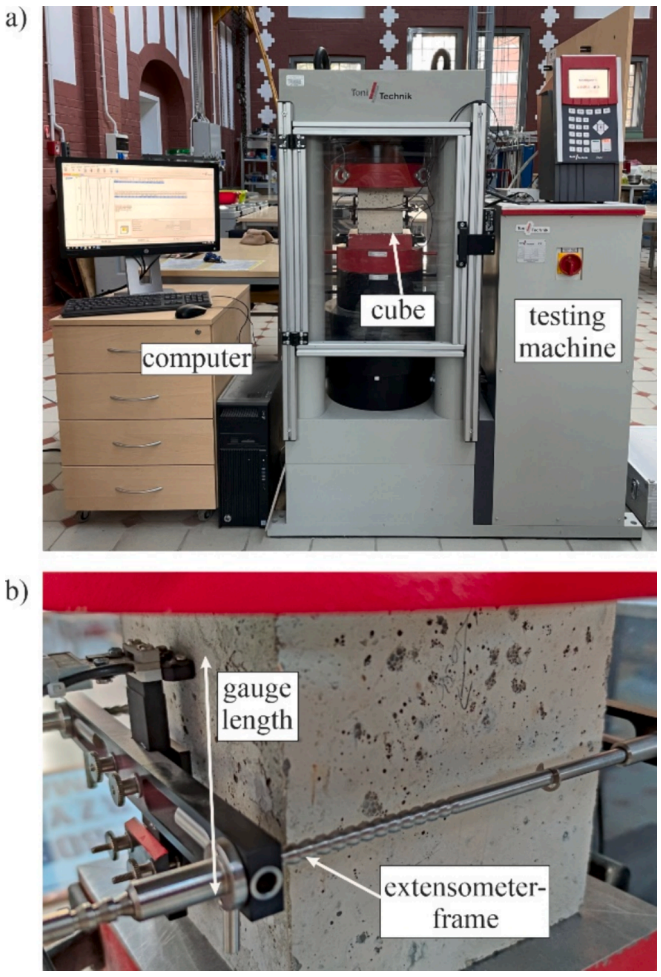

Fig. 4. Experimental setup for static test: (a) compression of the cube; (b) extensometer attached to the specimen.

parameters determined in this way are called the dynamic modulus of elasticity and dynamic Poisson's ratio. The relationship between static and dynamic moduli can be described by empirical relationships. The relationship between the static and dynamic Poisson's ratio is not clear, so the two parameters are usually assumed to be equal.

In this study, we have presented both approaches, static and dynamic testing. The first step was to perform a static compression test. Two tests were carried out, a cyclic test to determine the static elastic modulus and a standard compression test to determine the maximum stress value. The prepared cubes of dimensions 150 × 150 × 150 mm^3 were subjected to axial compression. The experiment was carried out using the load frame Toni Technik model 2091 (Fig. 4a). The secant modulus of elasticity was determined by cyclic testing according to method B of PN-EN 12390–13:2014–02 [35]. During the cyclic loading, the stress increase was controlled with a constant value of 0.3 MPa/s. The maximum stress level was assumed to be 16.7 MPa (about 25 % of maximum strength). The phases of no load and the maximum load lasted 20 s. Longitudinal deformations were recorded using a deformation measurement device equipped with a double extension sensor (two extensometers with a 75 mm gauge base, attached to the opposite sides of the cube, see Fig. 4b). Finally, the cube was compressed up to failure in a destructive test, with a speed of 0.6 MPa/s, to determine the compressive strength.

Fig. 5a shows the resulting stress-time curves, from which the static elastic modulus was obtained according to PN-EN 12390–13:2014–02. The stress–strain curve from the cyclic test is shown in Fig. 5b (blue line). As the destructive tests were carried out without an extensometer (to avoid destroying it), only the displacement of the crosshead was recorded. It is well known that the displacement of the crosshead cannot be used to calculate the deformation of the specimen, as such a result is subject to a large error. Therefore, the relationship between the actual strain (blue line) and the strain converted from the crosshead (magenta line) was established based on the cyclic test in which both the strains and displacements of the crosshead were recorded. By matching the curves, it was found that a strain multiplier of 1/4.5 was assumed for the testing machine used. Then, for the destructive test, the stress–strain curve (red line) was obtained using the same multiplier. On the basis of both compression tests, the following parameters were determined: the static elastic modulus $E_{st} = 27.42$ GPa and the failure stress $\sigma_{exp} = 66.0$ MPa.

Ultrasonic measurements were then performed to determine the dynamic parameters. Pressure and shear wave velocities of cubes (150 × 150 × 150 mm^3) were measured using a Pundit PL-200 device (Proceq) and ultrasonic transducers (Fig. 6). The ultrasonic pulse velocity (UPV) test was performed using two pairs of transducers. The first set consisted of two P-wave transducers with a frequency of 54 kHz, while the second set consisted of S-wave transducers with a frequency of 40 kHz. In order to determine the material parameters of concrete, the relationships for an isotropic medium between the bulk wave velocities (i.e. the P-wave velocity v_P and the S-wave velocity v_s) and the material constants (i.e. the mass density ρ, the dynamic elastic modulus of elasticity E_d and the Poisson's ratio ν) can be used:

$$v_P = \sqrt{\frac{E_d(1-\nu_d)}{\rho(1+\nu_d)(1-2\nu_d)}}, \quad v_S = \sqrt{\frac{E}{2\rho(1+\nu_d)}} \tag{8}$$

Based on the above relationships, one can obtain formulas for the dynamic elastic modulus of elasticity:

$$E_d = 2\rho v_S^2(1+\nu_d) \tag{9}$$

and the Poisson's ratio:

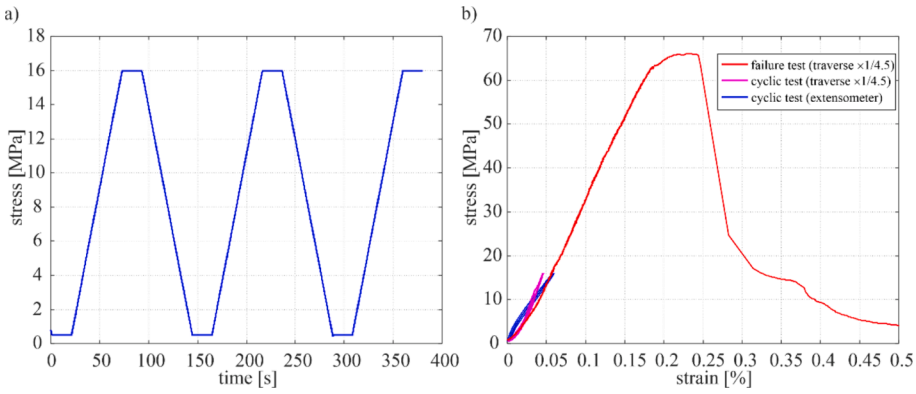

Fig. 5. Result of static compression test: (a) stress-time curve in the cyclic test, (b) stress–strain curves for cyclic and test and compression test up to failure.

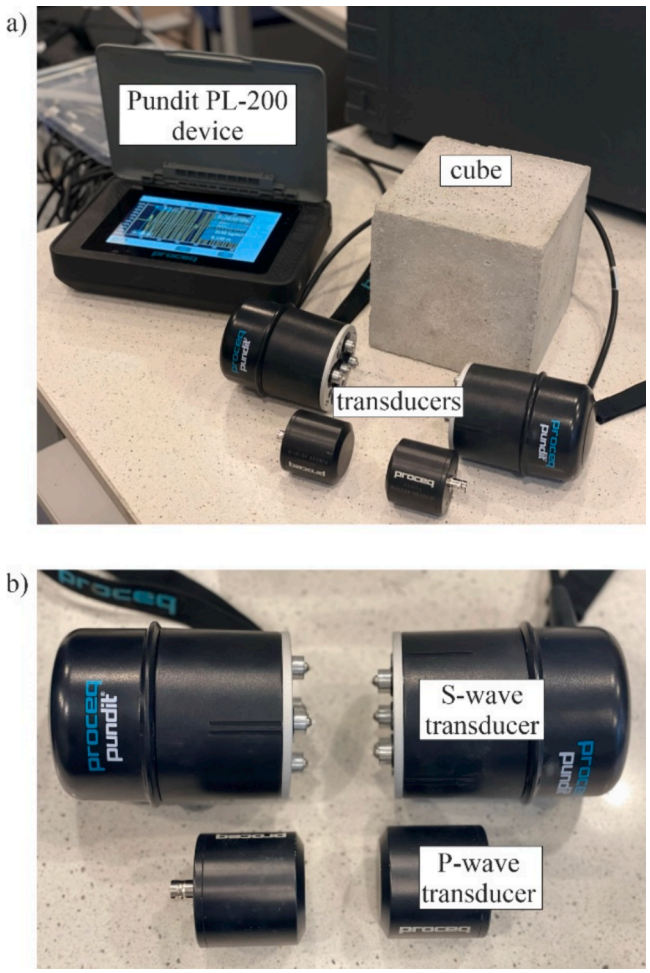

Fig. 6. Experimental setup for UPV test: (a) ultrasonic pulse analyser; (b) P-wave and S-wave transducers.

$$\nu_d = \frac{0.5\left(\frac{v_P}{v_S}\right)^2 - 1}{\left(\frac{v_P}{v_S}\right)^2 - 1} \tag{10}$$

Fig. 7 shows the results of the UPV test performed on the concrete cube. The P-wave signal is plotted with the blue line, while the S-wave signal is plotted with the red line. The distance between the transducers was 150 mm. The time-of-flight (TOF) identified was: $t_P = 35$ μs (for the P-wave) and $t_S = 55.1$ μs (for the S-wave). The dynamic elastic modulus and Poisson's ratio were calculated from Eqs. (9) and (10), and their values are: $E_d = 36.68$ GPa, $\nu_d = 0.16$, respectively.

Various empirical formulae have been proposed to find the relationship between the static modulus of elasticity E_{st} and the dynamic modulus of elasticity E_d [36]. Three methods are the most commonly used. The first is the relationship proposed by Lydon and Baledran [37]:

$$E_{st} = 0.83E_d \text{ [GPa]} \tag{11}$$

Another formula can be found in the British Standard BS8100 Part 2:

$$E_{st} = 1.25E_d - 19 \text{ [GPa]} \tag{12}$$

A formula incorporating the density of the concrete has been proposed by Popovics [38]:

$$E_{st} = \frac{446.09E_d^{1.4}}{\rho_c} \text{ [GPa]} \tag{13}$$

Table 1compares the E_{st} values calculated from Eqs. (11), (12) and (13) with the value obtained from the static cyclic test. The relative

Table 1
Comparison of the values of static elastic moduli.

Method	Lydon and Balendran	BS8100 Part 2	Popovics	Mean value	Static test
E_{st} [GPa]	30.44	26.85	32.46	29.92	27.42
Relative error [%]	11.0	2.1	18.4	9.1	–

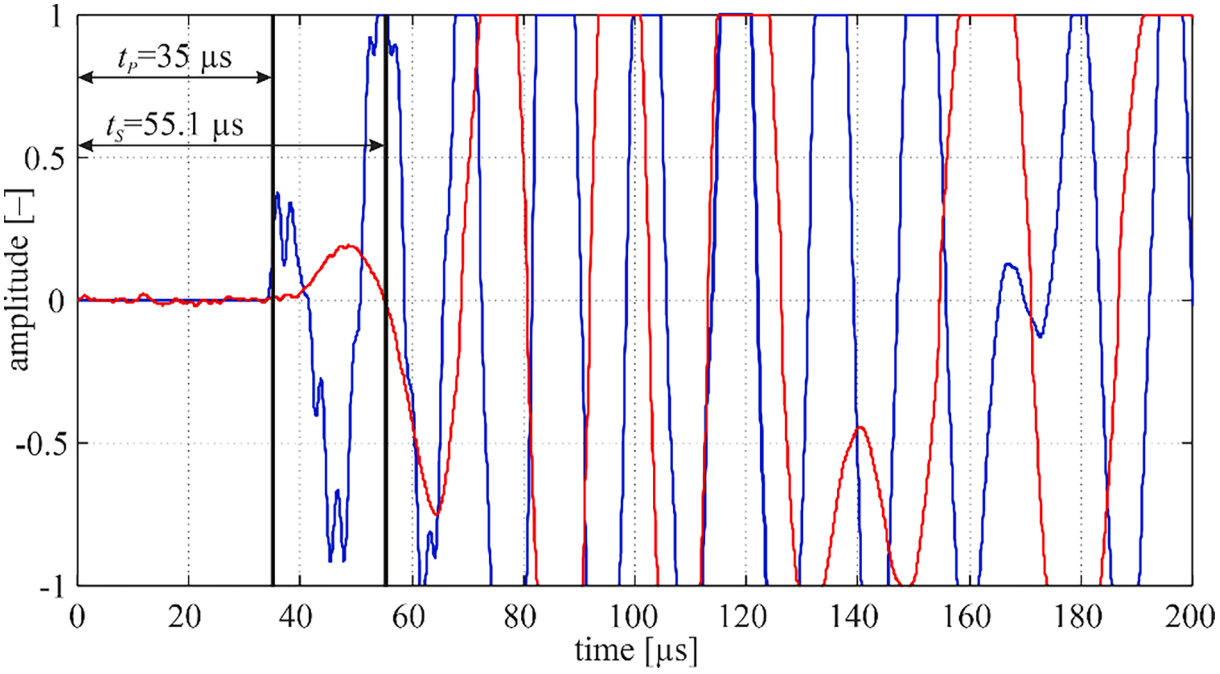

Fig. 7. Wave propagation signals registered by P-wave and S-wave transducers, with indicated TOF for primary and secondary waves (blue line – P-wave, red line – S-wave). (For interpretation of the references to colour in this figure legend, the reader is referred to the web version of this article.)

errors obtained are 2.1 % for the BS8100 method and 9.1 % for the mean value of these three methods, confirming the validity of this approach. The static Poisson's ratio ν_{st} was assumed to be the same as the dynamic ratio ν_d [39,40].

3.3. DEM numerical model

The numerical DEM analyses were performed on a cube with dimensions of 50 × 50 × 50 mm^3 (Fig. 8). As the sample consisted of 40,000 elements, resulting in almost 250,000 contacts, the number of global degrees of freedom was almost 1,500,000. The uniaxial and wave simulations tests were conducted for approximately 3 and 5 days, respectively, on Intel Xeon Platinum processors 8280 (2.70 GHz), without parallelization of the code. The particle diameter sizes were taken to be $d_{max} = 2$ mm and $d_{min} = 1.6$ mm. The maximum diameter was determined to correspond to the largest diameter of sand used in mortar concrete specimens, where gravel aggregates were not employed ([25,41]). The smaller elements significantly increase the computation time, but have a negligible effect on the results [42]. The density parameter ρ was chosen so that the mass of the model matched the actual mass. The particles were placed randomly with the aim of making the porosity of the model equal to the experimental $p = 7$ %. Although results may vary slightly depending on the arrangement, the differences are expected to be negligible, given the same sieve curve of the elements.

In contrast to the experimental measurements, a compression test was carried out numerically up to failure using vertical and horizontal virtual extensometers. The specimen was placed on the lower wall and the upper wall was moved at a constant velocity of 2.5 mm/s (the inertial number was kept below 10^{-4} to provide quasi-static conditions). Both walls were frictionless thus horizontal movement was possible. In the compression test, the parameters E_{dem} and ν_{dem} were chosen so that E_{glob} and ν_{glob} matched the actual values of E_{st} and ν_{st}. The calibrated values were equal to 23.31 GPa and 0.32, for E_{dem} and ν_{dem}, respectively, which corresponded to global values of $E_{glob} = 27.65$ GPa, $\nu_{glob} = 0.16$. The interparticle friction μ was equal to 18°. The normal contact strength T and shear cohesion C were both chosen to be 24.4 MPa. These values correspond to the maximum uniaxial compressive strength equal to σ_{dem} = 66.5 MPa. The correctness of the calculations carried out was confirmed by the consistency of the parameters obtained (Table 2) and the agreement of the slope of the curve obtained numerically with the experimental ones (Fig. 9).

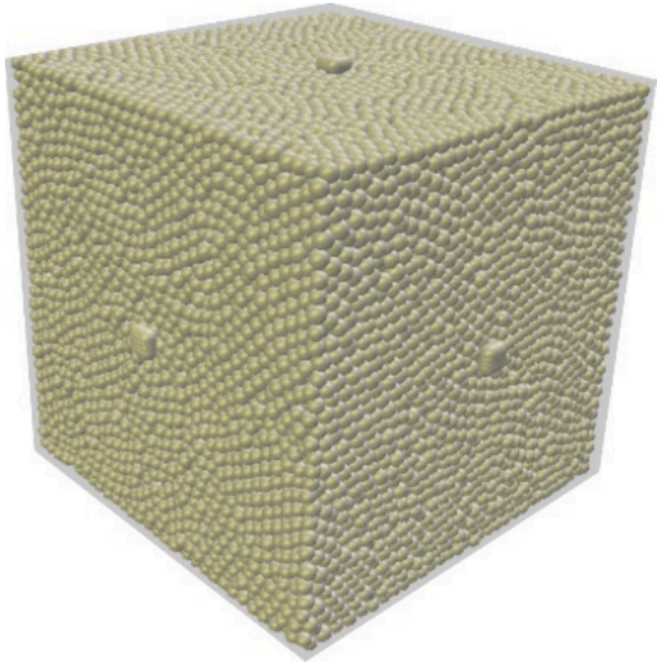

Fig. 8. Numerical DEM model of a concrete cube.

Table 2
Comparison of calibrated numerical global values and experimental ones.

	E_{glob} [GPa]	ν_{glob} [–]	σ_{dem} [MPa]
Experimental	27.42	0.16	66
Numerical	27.65	0.16	66.5

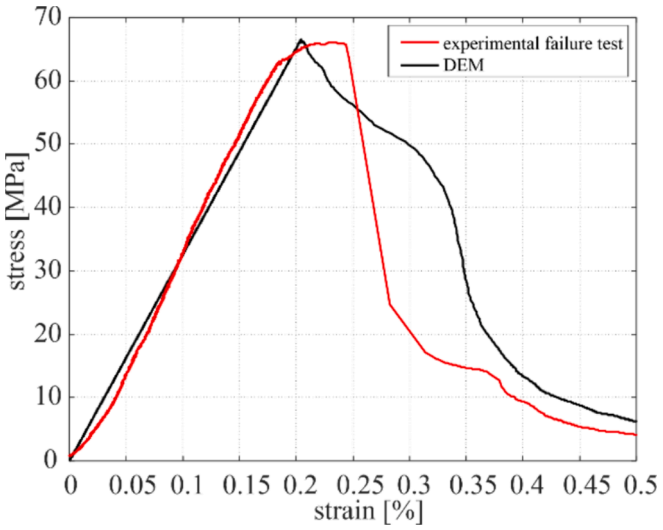

Fig. 9. Stress–strain curves for calibrated DEM model and experimental test.

4. Elastic wave propagation in concrete samples

4.1. Experimental setup for wave propagation

The measurements of elastic waves were carried out on cubes with edge lengths of 50 mm (Fig. 10). The piezoelectric plate transducers Noliac NAC2024 with dimensions of 3 × 3 × 3 mm^3 were used to excite and register the waves. One of the transducers acted as an actuator (A), while the others (B – G) acted as sensors. The location of the actuator and sensors is shown in Fig. 10b. The wave packet induced by the actuator was a five-cycle sine function modulated with a Hann window (Fig. 10c). The centre frequency of the wave packet was set in the frequency range of 100–500 kHz with a step of 50 kHz. The signals were further processed using the Hilbert transform to obtain signal envelopes [43].

4.2. Elastic wave propagation using DEM

After determining the crucial parameters calibrated to the experiment, it was possible to perform a simulation of elastic waves. The values of E_{dem} and ν_{dem} obtained by calibrating the model in the compression test were used. The equation of motion was integrated with a time step of $dt = 5{\cdot}10^{-8}$ s, up to 1.5 ms. In DEM calculations, the chosen time step is critical for the accuracy of the calculation. It can be estimated using the wave propagation velocity as $\Delta t_{cr} = \min(R_i\sqrt{\rho_i/E_i})$, where R_i is the radius of the sphere, ρ_i is the material density, and E_i is the Young modulus of contact for element "i". Taking into account the minimum radius of the sphere of 0.8 mm, the density of 2129.56 kg/m^3 and the Young modulus of the contact of 23.31 GPa, the critical time step Δt_{cr} equals $2.418{\cdot}10^{-7}$ s. However, in our study, the time step was further reduced to $5{\cdot}10^{-8}$ s to ensure accuracy in the propagation of elastic waves. A damping parameter of $\alpha_d = 1{\cdot}10^{-2}$ was used. In explicit

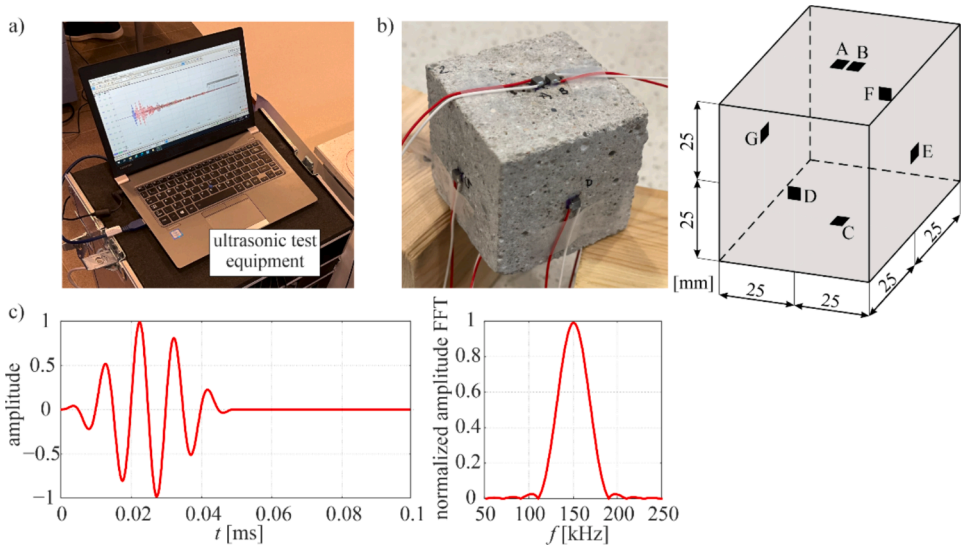

Fig. 10. Experimental setup (a); localization of PZT transducers (b); excitation signal in time and frequency domains (c).

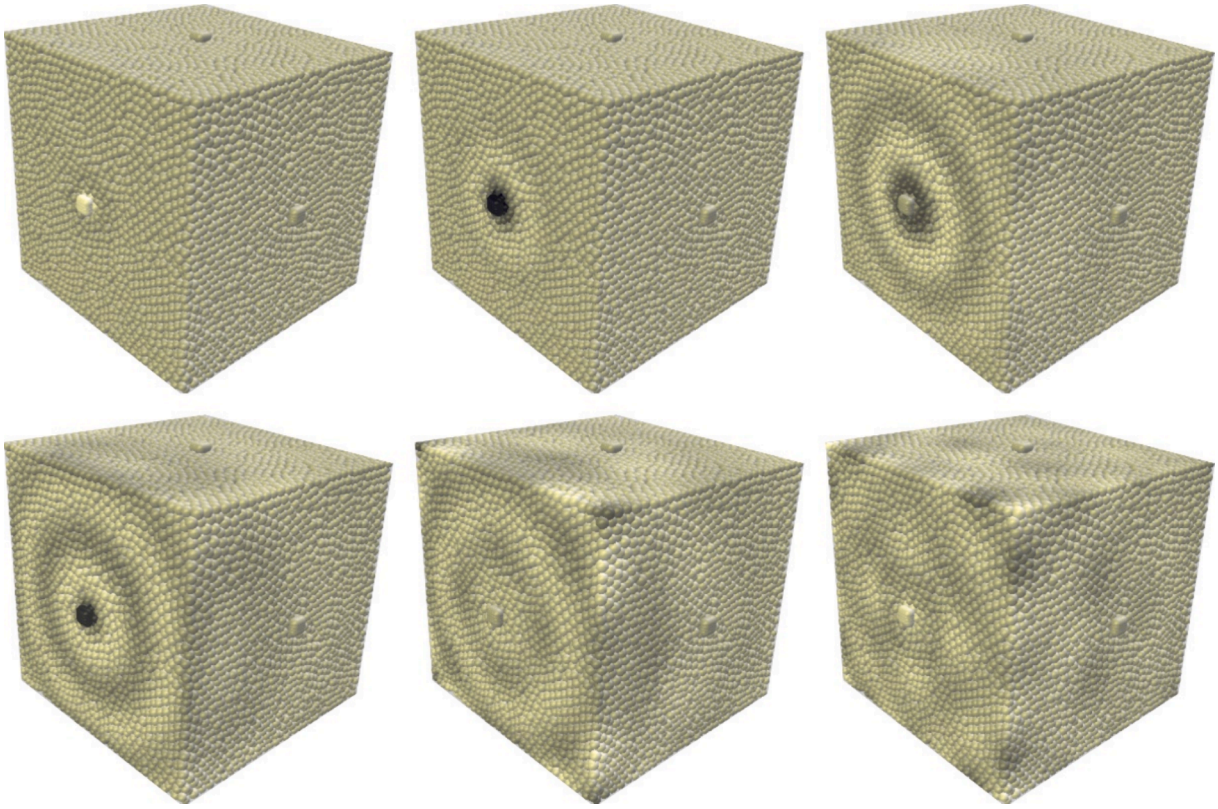

Fig. 11. Visualization of wave propagation in DEM model of concrete cube.

simulations, it is desirable to dissipate the kinetic energy of the particles. Since constitutive laws do not inherently include velocity-based damping, artificial numerical damping can be used. However, in dynamic studies, the numerical damping should be small enough to neglect its effects. After some numerical experiments using a trial-and-error technique, a damping coefficient of $\alpha_d = 1{\cdot}10^{-2}$ was chosen, which affected the wave propagation results by less than 1 %. The interaction zone was characterised by a contact factor $Cf = 1.1$. This zone corresponds to the radius of contact for each particle. The signal was excited by actuator A and received by virtual sensors B-G, placed as in the experiment. The wave was excited as a five-cycle sine function which was set in the frequency range of 100–500 kHz with a step of 50 kHz. Fig. 11 shows snapshots illustrating the propagation of the disturbance in the DEM model of the concrete cube, at selected time instances. The wave starts to propagate at the centre of the left surface and then spreads throughout the sample. Acceleration signals of a length of 1.5 ms were recorded at the location of sensors B-D and then compared with the experimental signals in the following section.

4.3. Experimental and numerical results of wave propagation

In this section, the numerical and experimental signals of elastic waves propagating in the concrete cube are compared. Fig. 12 shows the signals recorded during the experiment. In an ideal situation

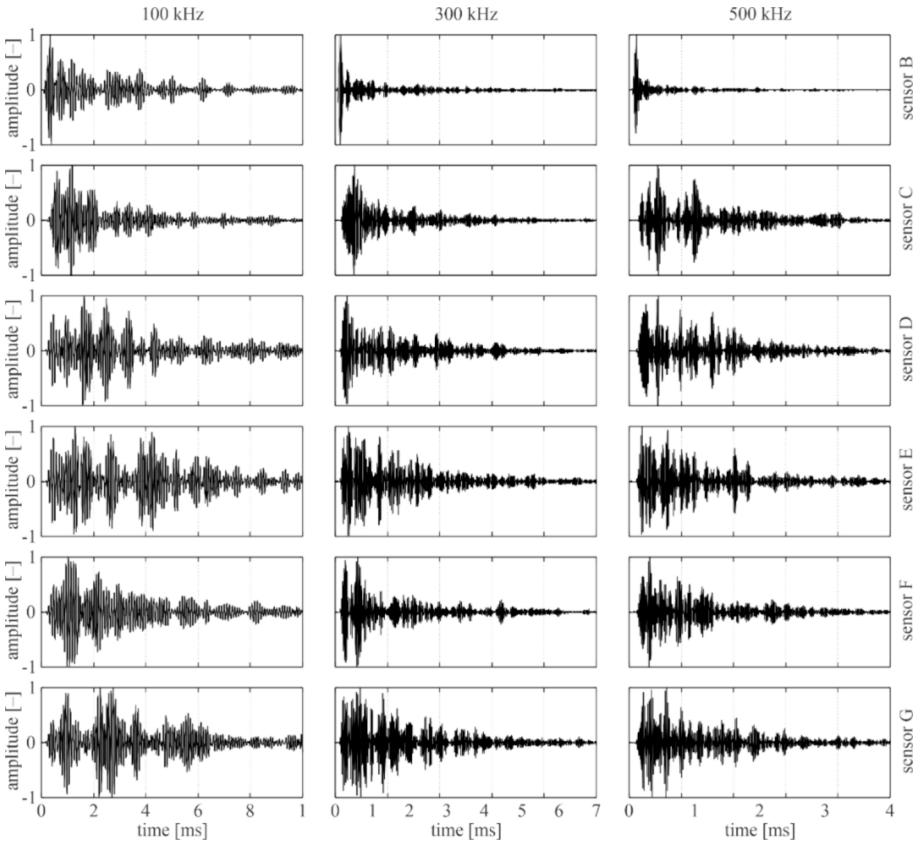

Fig. 12. Experimental wave propagation signals in time domain registered by sensors B to G.

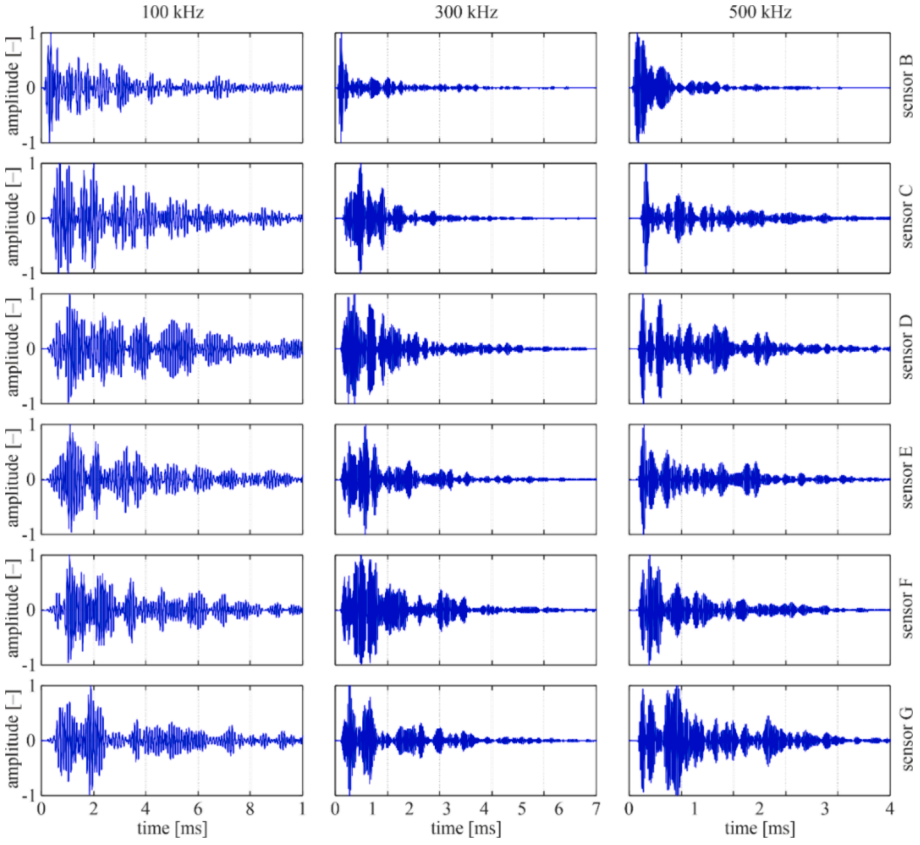

Fig. 13. Numerical wave propagation signals in time domain registered by sensors B to G.

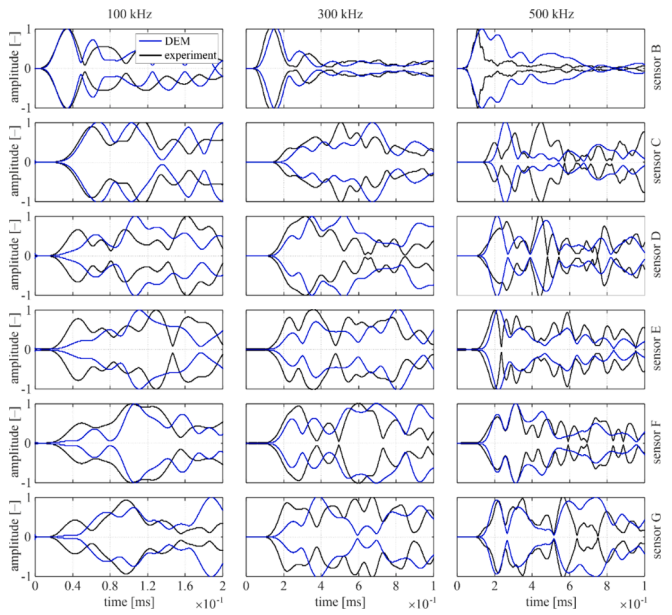

Fig. 14. Comparison of experimental and numerical signal envelopes in the time domain for the first few wave packets.

(homogeneous material, ideal positioning of the sensors) the individual signals recorded by the sensors placed on opposite sides should be the same, i.e. G = E and F = D. However, in real conditions, it is not possible to achieve perfect consistency and differences in the signals can be observed. The main factors influencing these differences are: heterogeneity of the sample structure, variations in sample dimensions and inaccuracy in the arrangement and location of the sensors.

Fig. 13 shows the numerical wave propagation signals. As in the experiment, there are differences between the G-E and F-D signals. In contrast to the experimental approach, the numerical cube has exactly the same dimensions and sensor locations. The differences observed are therefore due to the structure of the numerical model. The cubes are created by arranging spherical elements in a random pattern, creating inhomogeneity and causing differences in the recorded wave signals. As a result, elastic waves can exhibit variations in propagation in different directions. While the sieve curve (mainly d_{max}) remains unchanged, the results may vary slightly for different random distributions of spheres due to heterogeneity. Although the results would not be identical, the averages should converge for a large number of random calculations. However, including *meso*-scale features such as aggregates, mortar, and air voids in the model can increase the heterogeneity of the specimen. This would lead to even greater disturbances in wave propagation, resulting in better agreement with reality.

Fig. 14 shows the envelopes of the signals obtained, both experimentally and numerically. The waveforms have been zoomed in to

Table 3
Pearson correlation coefficient between experimental and numerical wave propagation signals in relation to excitation frequency.

frequency [kHz]	100	150	200	250	300	350	400	450	500
PCC [–]	0.68	0.72	0.70	0.74	0.75	0.70	0.74	0.73	0.70

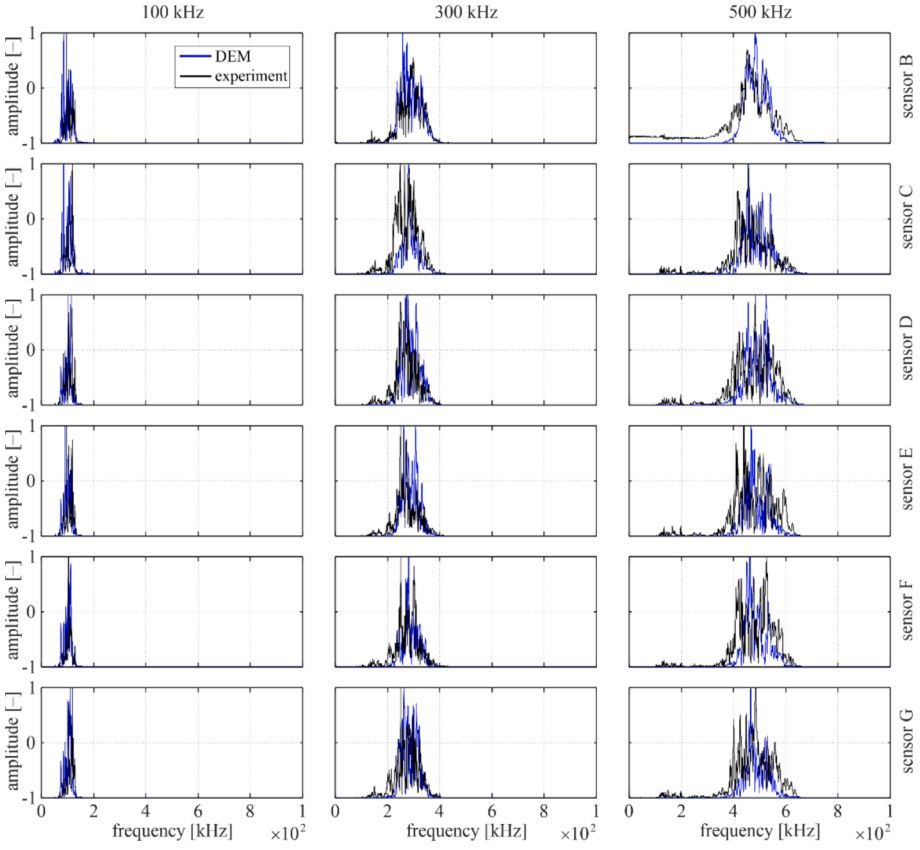

Fig. 15. Comparison of experimental and numerical signals in the frequency domain.

highlight the beginnings of the signals. By analysing the plots, it is possible to observe the compatibility of the shape of the wave packets.

Despite slight differences in the corresponding experimental and numerical signals, a global agreement between the obtained signals is evident. The compatibility between the experimental and numerical signals was checked by calculating the Pearson Correlation Coefficient (PCC). The mean PCC values (for all sensors) in relation to the excitation frequency are presented in Table 3. A good agreement can be observed. As the PCC value is higher than 0.7, it can be considered as a strong correlation [44]. The obtained PCC values confirm the correctness of the calibrated mechanical parameters as well as the selected damping factor α_d.

An important aspect of verifying the accuracy of the computational model is to compare the recorded experimental and numerical signals in the frequency domain. Fig. 15 presents Fourier transforms calculated for all sensors B – G and selected frequencies (100, 300, 500 kHz). It can be seen that the experimental and numerical spectra are concentrated around the excitation frequency.

5. Conclusions

The presented paper investigated the modelling of wave propagation in a *meso*-scale model of concrete. The experimental and numerical tests were conducted on concrete cubic samples. The wave propagation experiment was simulated in a DEM environment.

A key achievement of the research carried out was to propose a novel methodology for constructing a *meso*-scale model of concrete dedicated to elastic wave propagation analysis. Experimental tests required to determine the static mechanical parameters, i.e., the static Young modulus and static Poisson's ratio were described. It was proven that static parameters can also be determined by dynamic testing and the application of appropriate empirical formulae. The calibration of the mechanical parameters of the DEM model to match the experimental values involved linking local, micro-parameters between particles to the global response of the whole sample. Due to calibration conducted by numerical compression test up to failure, the local parameters were identified in such a way that the global parameters matched the values of the static Young modulus and static Poisson's ratio.

The developed numerical model was further used to simulate the propagation of elastic waves in a concrete cubic sample, in the frequency range of 100–500 kHz. The results of the DEM calculations exhibited good agreement with the experimental ultrasonic signals. The compatibility between the experimental and numerical signals checked by calculating the PCC revealed a strong correlation in the analysed frequency range.

This study takes the first step towards the investigating the phenomena of elastic wave propagation in heterogeneous materials. This knowledge is essential for further studies on the application of ultrasonic waves in fracture monitoring and explaining their interaction with micro- and macro-cracking of concrete elements. Further work will focus on more advanced DEM models, including real shaped aggregates and modelling of wave propagation during mechanical degradation of samples for early damage detection.

CRediT authorship contribution statement

Magdalena Knak: Visualization, Writing – original draft, Methodology, Investigation, Formal analysis, Conceptualization. **Michał Nitka:** Writing – original draft, Methodology, Investigation, Formal analysis, Conceptualization. **Magdalena Rucka:** Writing – review & editing, Writing – original draft, Supervision, Project administration, Methodology, Investigation, Funding acquisition, Formal analysis, Conceptualization.

Declaration of competing interest

The authors declare that they have no known competing financial interests or personal relationships that could have appeared to influence the work reported in this paper.

Data availability

Data will be made available on request.

Acknowledgements

The study was financed by the National Science Centre, Poland, under the project "Complex investigations of the development of micro- and macro-cracks in concrete members using elastic waves: experiments and discrete element method modelling" no 2019/35/B/ST8/01905.

References

[1] M. Zielińska, M. Rucka, Imaging of Increasing Damage in Steel Plates Using Lamb Waves and Ultrasound Computed Tomography. Materials (Basel) 2021, 5114. doi: 10.3390/ma14175114.
[2] Ł. Pieczonka, Ł. Ambroziński, W.J. Staszewski, D. Barnoncel, P. Pérès, Damage detection in composite panels based on mode-converted Lamb waves sensed using 3D laser scanning vibrometer, Opt Lasers Eng 99 (2017) 80–87, https://doi.org/10.1016/j.optlaseng.2016.12.017.
[3] T. Wandowski, M. Radzienski, D. Mindykowski, P. Kudela, Analysis of damage localisation results in GFRP panel for different configurations of air-coupled transducers, Ultrasonics 132 (2023) 106986, https://doi.org/10.1016/j.ultras.2023.106986.
[4] E. Wojtczak, M. Rucka, Damage imaging algorithm for non-destructive inspection of CFRP/steel adhesive joints based on ultrasonic guided wave propagation, Compos Struct 297 (2022) 115930, https://doi.org/10.1016/j.compstruct.2022.115930.
[5] T. Tong, J. Hua, F. Gao, J. Lin, Identification of bolt state in lap joint based on propagation model and imaging methods of Lamb waves, Mech Syst Signal Process 200 (2023) 110569, https://doi.org/10.1016/j.ymssp.2023.110569.
[6] Z. Yang, H. Yang, T. Tian, D. Deng, M. Hu, J. Ma, et al., A review in guided-ultrasonic-wave-based structural health monitoring: From fundamental theory to machine learning techniques, Ultrasonics 133 (2023) 107014, https://doi.org/10.1016/j.ultras.2023.107014.
[7] R. Jasiński, Identification of Stress States in Compressed Masonry Walls Using a Non-Destructive Technique (NDT), Materials (basel) 13 (2020) 2852, https://doi.org/10.3390/ma13122852.
[8] K. Schabowicz, Modern acoustic techniques for testing concrete structures accessible from one side only, Arch Civ Mech Eng 15 (2015) 1149–1159, https://doi.org/10.1016/j.acme.2014.10.001.
[9] X. Wang, E. Niederleithinger, I. Hindersmann, The installation of embedded ultrasonic transducers inside a bridge to monitor temperature and load influence using coda wave interferometry technique, Struct Heal Monit 21 (2022) 913–927, https://doi.org/10.1177/14759217211014430.
[10] K.J. Vössing, M. Gaal, E. Niederleithinger, Imaging wood defects using air coupled ferroelectret ultrasonic transducers in reflection mode, Constr Build Mater (2020) 241, https://doi.org/10.1016/j.conbuildmat.2020.118032.
[11] M. Zielińska, M. Rucka, Assessment of Wooden Beams from Historical Buildings Using Ultrasonic Transmission Tomography, Int J Archit Herit 17 (2023) 249–261, https://doi.org/10.1080/15583058.2022.2086505.
[12] J.D. Rodríguez-Mariscal, J. Canivell, M. Solís, Evaluating the performance of sonic and ultrasonic tests for the inspection of rammed earth constructions, Constr Build Mater (2021) 299, https://doi.org/10.1016/j.conbuildmat.2021.123854.
[13] James F. Doyle. Wave Propagation in Structures. An FFT-Based Spectral Analysis Methodology. Springer New York, NY; 1989. DOI: DOI: 10.1007/978-1-4684-0344-2.
[14] M. Palacz, Spectral methods for modelling of wave propagation in structures in terms of damage detection - A review, Appl Sci (2018) 8, https://doi.org/10.3390/app8071124.
[15] M.B. Hafeez, M. Krawczuk, A Review: Applications of the Spectral Finite Element Method, Arch Comput Methods Eng 30 (2023) 3453–3465, https://doi.org/10.1007/s11831-023-09911-2.
[16] P. Kudela, Parallel implementation of spectral element method for Lamb wave propagation modeling, Int J Numer Methods Eng 106 (2016) 413–429, https://doi.org/10.1002/nme.5119.
[17] K. Askaripour, A. Żak, A study on diagnosing both isotropic and orthotropic, intentionally damaged laminates, Nondestruct Test Eval 36 (2021) 237–260, https://doi.org/10.1080/10589759.2020.1740701.
[18] P. Fiborek, R. Soman, P. Kudela, W. Ostachowicz, Spectral element modeling of ultrasonic guided wave propagation in optical fibers, Ultrasonics 124 (2022), https://doi.org/10.1016/j.ultras.2022.106746.
[19] M. Rucka, W. Witkowski, J. Chróścielewski, S. Burzyński, K. Wilde, A novel formulation of 3D spectral element for wave propagation in reinforced concrete,

Bull Polish Acad Sci Tech Sci 65 (2017) 805–813, https://doi.org/10.1515/bpasts-2017-0089.
[20] A. Asadollahi, L. Khazanovich, Numerical investigation of the effect of heterogeneity on the attenuation of shear waves in concrete, Ultrasonics 91 (2019) 34–44, https://doi.org/10.1016/j.ultras.2018.07.011.
[21] T. Yu, J.F. Chaix, L. Audibert, D. Komatitsch, V. Garnier, J.M. Hénault, Simulations of ultrasonic wave propagation in concrete based on a two-dimensional numerical model validated analytically and experimentally, Ultrasonics 92 (2019) 21–34, https://doi.org/10.1016/j.ultras.2018.07.018.
[22] B. Xu, H. Chen, Y.L. Mo, T. Zhou, Dominance of debonding defect of CFST on PZT sensor response considering the meso-scale structure of concrete with multi-scale simulation, Mech Syst Signal Process 107 (2018) 515–528, https://doi.org/10.1016/j.ymssp.2018.01.041.
[23] H. Chen, B. Xu, J. Wang, L. Luan, T. Zhou, X. Nie, et al., Interfacial debonding detection for rectangular cfst using the masw method and its physical mechanism analysis at the meso-level, Sensors (switzerland) (2019) 19, https://doi.org/10.3390/s19122778.
[24] C. Xie, L. Yuan, M. Zhao, Y. Jia, Study on failure mechanism of porous concrete based on acoustic emission and discrete element method, Constr Build Mater 235 (2020) 117409, https://doi.org/10.1016/j.conbuildmat.2019.117409.
[25] M. Nitka, J. Tejchman, Comparative DEM calculations of fracture process in concrete considering real angular and artificial spherical aggregates, Eng Fract Mech 239 (2020) 107309, https://doi.org/10.1016/j.engfracmech.2020.107309.
[26] M. Nitka, J. Tejchman, Meso-mechanical modelling of damage in concrete using discrete element method with porous ITZs of defined width around aggregates, Eng Fract Mech 231 (2020) 107029, https://doi.org/10.1016/j.engfracmech.2020.107029.
[27] J. Suchorzewski, M. Nitka, Size effect at aggregate level in microCT scans and DEM simulation – Splitting tensile test of concrete, Eng Fract Mech 264 (2022) 108357, https://doi.org/10.1016/j.engfracmech.2022.108357.
[28] R. Zhu, S.Y. Alam, A. Loukili, Relevance of displacement softening model in discrete element method to investigate structural and grain size scaling effect, Theor Appl Fract Mech 123 (2023) 103706, https://doi.org/10.1016/j.tafmec.2022.103706.
[29] M.H. Sadd, G. Adhikari, F. Cardoso, DEM simulation of wave propagation in granular materials, Powder Technol 109 (2000) 222–233, https://doi.org/10.1016/S0032-5910(99)00238-7.
[30] M. Nishida, K. Tanaka, T. Ishida, DEM simulation of wave propagation in two-dimensional ordered array of particles. Shock Waves 26th Int, Symp. Shock Waves 2 (2009) 815–820, https://doi.org/10.1007/978-3-540-85181-3_3.
[31] J. Rojek, N. Madan, S. Nosewicz, Micro-Macro Relationships in the Simulation of Wave Propagation Phenomenon Using the Discrete Element Method, Materials (basel) 12 (2019) 4241, https://doi.org/10.3390/ma12244241.
[32] J. Kozicki, F.V. Donzé, A new open-source software developed for numerical simulations using discrete modeling methods, Comput Methods Appl Mech Eng 197 (2008) 4429–4443, https://doi.org/10.1016/j.cma.2008.05.023.
[33] P.A. Cundall, O.D.L. Strack, A discrete numerical model for granular assemblies, Geotechnique 29 (1979) 47–65.
[34] V. Šmilauer, B. Chareyre, Yade DEM Formulation, 1st ed., Yade Doc, The Yade Project, 2010.
[35] J. Michałek, Wyznaczanie modułu sprężystości betonu przy ściskaniu, Mater Bud 1 (2015) 66–67, https://doi.org/10.15199/33.2015.06.23.
[36] B.J. Lee, S.H. Kee, T. Oh, Y.Y. Kim, Evaluating the Dynamic Elastic Modulus of Concrete Using Shear-Wave Velocity Measurements. Adv, Mater Sci Eng (2017; 2017.), https://doi.org/10.1155/2017/1651753.
[37] F.D. Lydon, R.V. Balendran, Some observations on elastic properties of plain concrete, Cem. Concr. Res. 16 (1986) 314–324, https://doi.org/10.1016/0008-8846(86)90106-7.
[38] S. Popovics, Verification of relationships between mechanical properties of concrete-like materials, Matériaux Constr 8 (1975) 183–191, https://doi.org/10.1007/BF02475168.
[39] Marques AI, Morais J, Morais P, Veiga M do R, Santos C, Candeias P, et al. Modulus of elasticity of mortars: Static and dynamic analyses. Constr Build Mater 2020;232: 117216. DOI: 10.1016/j.conbuildmat.2019.117216.
[40] E. Wojtczak, M. Rucka, Monitoring the curing process of epoxy adhesive using ultrasound and Lamb wave dispersion curves, Mech Syst Signal Process 151 (2021) 107397, https://doi.org/10.1016/j.ymssp.2020.107397.
[41] Ł. Skarżyński, M. Nitka, J. Tejchman, Modelling of concrete fracture at aggregate level using FEM and DEM based on X-ray μCT images of internal structure, Eng Fract Mech 147 (2015) 13–35, https://doi.org/10.1016/j.engfracmech.2015.08.010.
[42] J. Suchorzewski, J. Tejchman, M. Nitka, Discrete element method simulations of fracture in concrete under uniaxial compression based on its real internal structure, Int J Damage Mech 27 (2018) 578–607, https://doi.org/10.1177/1056789517690915.
[43] C.T. Ng, On the selection of advanced signal processing techniques for guided wave damage identification using a statistical approach, Eng. Struct. 67 (2014) 50–60, https://doi.org/10.1016/j.engstruct.2014.02.019.
[44] P. Schober, L.A. Schwarte, Correlation coefficients: Appropriate use and interpretation, Anesth. Analg. 126 (2018) 1763–1768, https://doi.org/10.1213/ANE.0000000000002864.